Contemporary Mathematics
https://ojs.wiserpub.com/index.php/CM/

Research Article

Mathematical Modelling and Computational Simulation of Oxy-Combustion Carbon Capture Using Ion-Transport Membranes

Rached Ben-Mansour[1,2]

[1] Department of Mechanical Engineering, King Fahd University of Petroleum and Minerals, Dhahran 31261, Saudi Arabia
[2] Interdisciplinary Research Center for Sustainable Energy Systems, King Fahd University of Petroleum and Minerals, Dhahran 31261, Saudi Arabia
E-mail: rmansour@kfupm.edu.sa

Received: 30 September 2025; **Revised:** 27 February 2026; **Accepted:** 5 March 2026

Abstract: Global warming is the most challenging environmental problem and is expected to remain so for the next few decades. In June 2025, scientists predicted that it would be extremely difficult to meet the 2030 global temperature reduction milestone. Therefore, it is necessary to double our efforts to reduce global warming through several approaches, including higher renewable energy usage, energy efficiency, and carbon capture. Mathematical modelling and computational simulation are important tools for modelling complex processes that occur in important environmental applications such as carbon capture. In this paper, we present the mathematical modelling of a carbon capture method that allows simultaneous oxygen production and combustion, to allow direct carbon capture after water vapor condensation. The study lays out the development of an oxy-fuel combustion model integrated with an oxygen separation model in two mini-reactors. The model has been validated against recent experimental oxyfuel combustion in a button-cell reactor, and very good agreement has been obtained. The normalized Root Mean Square (RMS) value for the difference between the experimental and predicted results of the permeated oxygen for nonreactive cases was around 4%, and for the reactive cases 6% respectively. The validated model was used to simulate oxygen separation and oxyfuel combustion in annular reactors that can be used for carbon capture in industrial applications as one of the solutions to fight global warming. It was found that it is more efficient to have the air flow in the inner tube for air velocities ranging between 0.05 to 2 m/s. As the sweep velocity increased from 0.05 to 2.5 m/s, the separated oxygen mass flow rate increased by a factor of 5 or higher. For the reacting cases, feeding 2% methane oxy-combustion has increased the oxygen permeation by as much as 17% for annular oxy-combustion cases and by 12% for tubular oxy-combustion cases. The sweeping gas velocity increase seems to be more effective in increasing the oxygen permeation. This effect is still valid under reacting cases.

Keywords: Ion Transport Membrane (ITM), oxyfuel, zero-carbon, mathematical modelling, $Ba_{0.5}Sr_{0.5}Co_{0.8}Fe_{0.2}O_{3-\delta}$ (BSCF), Computational Fluid Dynamics (CFD)

MSC: 76M12, 80A25, 76V05

DOI: https://doi.org/10.37256/cm.7320268781

Nomenclature

Abbreviations

BBCF	$\mathrm{BaBi_{0.4}Co_{0.2}Fe_{0.4}O_{3-\delta}}$ (Barium-Bismuth-Cobalt-Iron-Oxide)
BCF	$\mathrm{BaCe_{0.15}Fe_{0.85}O_{3-\delta}}$ (Barium-Cerium-Cobalt-Iron-Oxide)
BSCF	$\mathrm{Ba_{0.5}Sr_{0.5}Co_{0.8}Fe_{0.2}O_{3-\delta}}$ (Barium-Strontium-Cobalt-Iron-Oxide)
BSCFO	$\mathrm{Ba_{0.5}Sr_{0.5}Co_{0.8}Fe_{0.2}O_{3-\delta}}$ (same as BSCF)
BSCF tube	$\mathrm{Ba_{0.5}Sr_{0.5}Co_{0.8}Fe_{0.2}O_{3-\delta}}$ in tube form (other materials in plate form)
BTCF	$\mathrm{BaTi_{0.2}Co_{0.5}Fe_{0.3}O_{3-\delta}}$ (Barium-Titanium-Cobalt-Iron-Oxide)
CFD	Computational Fluid Dynamics
CLFC	$\mathrm{Ca_{0.6}La_{0.4}Fe_{0.75}Co_{0.25}O_{3-\delta}}$ (Calcium-Lanthanum-Iron-Cobalt-Oxide)
ITM	Ion Transport Membrane
KFUPM	King Fahd University for Petroleum and Minerals
LCFC	$\mathrm{La_{0.6}Ca_{0.4}Fe_{0.75}Co_{0.25}O_{3-\delta}}$ (Lanthanum-Calcium-Iron-Cobalt-Oxide)
LCFC tube	$\mathrm{La_{0.6}Ca_{0.4}Fe_{0.75}Co_{0.25}O_{3-\delta}}$ in tube form
LNO	Lanthanum-Nickel-Oxide
LaSrCoO	Lanthanum-Strontium-Cobalt-Oxide
LSC	$\mathrm{La_{0.5}Sr_{0.5}CoO_{3-\delta}}$ (Lanthanum-Strontium-Cobalt-Oxide)
LSCF	$\mathrm{La_{0.6}Sr_{0.4}Co_{0.2}Fe_{0.8}O_{3-\delta}}$ (Lanthanum-Strontium-Cobalt-Iron-Oxide)
LSCF 950 C	$\mathrm{La_{0.6}Sr_{0.4}Co_{0.2}Fe_{0.8}O_{3-\delta}}$ at 950 °C (all other materials at 875 °C in Figure 1)
LSGF	$\mathrm{La_{0.15}Sr_{0.85}Ga_{0.3}Fe_{0.7}O_{3-\delta}}$ (Lanthanum-Strontium-Gallium-Iron-Oxide)
LSGF-BSCF	$\mathrm{12.8La_{0.15}Sr_{0.85}Ga_{0.3}Fe_{0.7}O_{3-\delta}\text{-}Ba_{0.5}Sr_{0.5}Fe_{0.2}Co_{0.8}Fe_{0.2}O_{3-\delta}}$
mOTS	Mini-Oxygen Transport Separator
mOTR	Mini-Oxygen Transport Reactor
PDEs	Partial Differential Equations
SrCeFeO	Strontium-Cerium-Iron-Oxide
SrCoFeO	Strontium-Cobalt-Iron-Oxide
SFN	$\mathrm{SrFe_{0.8}Nb_{0.2}O_{3-\delta}}$

Roman symbols

Symbol	Description	SI Unit
Cp	Specific heat	J/(Kg·K)
D_i	Inner diameter of mOTS	m or mm
D_o	Outer diameter of mOTS	m or mm
$D_{i,m}$	Diffusion coefficient of the i^{th} specie	$\mathrm{m^2/s}$
D_v	Oxygen vacancy diffusion coefficient	$\mathrm{m^2/s}$
I	Total radiation intensity	$\mathrm{W\cdot m^{-2}\cdot sr^{-1}}$
J_{O2}	Flux of permeated oxygen	$\mathrm{mol\cdot m^{-2}s^{-1}}$
k_{eff}	Mixture effective thermal conductivity	$\mathrm{W\cdot m^{-1}K^{-1}}$
k_f	Forward reaction rate constant for ITM	$\mathrm{m\cdot Pa^{-1}s^{-1}}$
k_r	Reverse reaction rate constant for ITM	$\mathrm{mol\cdot m^{-2}s^{-1}}$
L	Length of mOTS/mOTR	m
L_m	Thickness of membrane	m
$\dot{m}_{O_2}$	Mass flow rate of separated oxygen	Kg/s
P	Pressure	Pa
P_1	Feed side oxygen partial pressure	Pa
P_2	Sweep side oxygen partial pressure	Pa
$\vec{r}$	directional vector	Magnitude in m
$\vec{s}$	directional vector	Magnitude in m

S_i	Source term for species i	$Kg{\cdot}m^{-3}s^{-1}$
T	Temperature	K or °C
U	Velocity vector	Magnitude in m/s
$\overline{V}_{air}$	Average air velocity	m/s
$\overline{V}_{CO_2}$	Average velocity of CO_2	m/s
Y_i	Mass fraction of specie i	kg of O_2/kg of mixture

Greek symbols

κ	Absorption coefficient	m^{-1}
ρ	Density	kg/m^3
μ	Dynamic viscosity	$N{\cdot}s{\cdot}m^{-2}$
∇	Gradient operator	
σ	Stefan-Boltzmann constant	$W{\cdot}m^{-2}K^{-4}$

1. Introduction

Ion Transport Membranes (ITM) have been proposed as a novel technology for oxygen separation and in-situ oxy-fuel combustion. Oxy-fuel combustion is one of three methods that allow easy capture of CO_2 and, hence, help in reducing greenhouse gases. In this study, we investigate the separation productivity of cylindrical ITMs in cross flow using state of the art Computational Fluid Dynamics (CFD) method. The productivity of oxygen separation in ITM has a strong relation to the partial pressure difference between the feed and permeate sides of the membrane. In this application, the sweeping of an inert gas is used to remove the permeated oxygen and lower the partial pressure on the permeation side. Therefore, the control of the flow on both the feed and the permeate sides is a very important factor in increasing the permeated oxygen flux.

In this study, we take another look at the results of a compact mini-separator, including the effect of sweeping velocity, and we present the results of mini-reactors. Mini-separators or mini-reactors with a cylindrical shape (a few mm in diameter) that enable oxygen separation or oxy-fuel combustion carbon capture technology to be implemented in a reasonably sized combustion chamber for power generation applications and/or gas turbine applications. Binash [1] conducted thermodynamic analysis and exergetic analysis for a modified gas turbine power generation cycle and has shown that the integration of ITM technology is competitive with current regular technologies. Another driving cause for choosing mini-circular tubes Oxygen Transport Reactor (OTR) is the fact that BSCF tubes have shown the best performance, as shown in Figure 1 taken from Foy and McGovern [2]. Felice et al. [3] have worked on fibrous BSCF tubes with thicknesses of 0.2 and 0.5 mm and discussed methods of sealing them for practical application purposes.

Different modelling methods have been adopted for the simulation of oxygen transport through Ion-Transport Membranes. The model equations used for oxygen permeation in membranes are summarized in Table 1 below. The models represent the transport modes of oxygen through a given membrane. The possible modes of transport include a) advective transport of oxygen through the boundary layer close to the boundary on the air side, b) adsorption of oxygen by the surface of the membrane, c) diffusion of oxygen ions (and electrons) through the membrane thickness and d) desorption (after ion-electron recombination) of oxygen and e) advective transport of the oxygen on permeate side of the membrane. The advective transport is automatically taken care of through the solution of the flow and species transport. The membrane model in a detailed Computational Fluid Dynamics (CFD) model should include only processes b, c, and d. Some models include the three processes, and other models do not. The best model that includes all the different steps of oxygen permeation through an ITM is the comprehensive model of Xu and Thomson [4]. Later, Xu and Thomson's [4] model have been modified to allow for a two-step reaction as explained by Behrouzifar et al. [5].

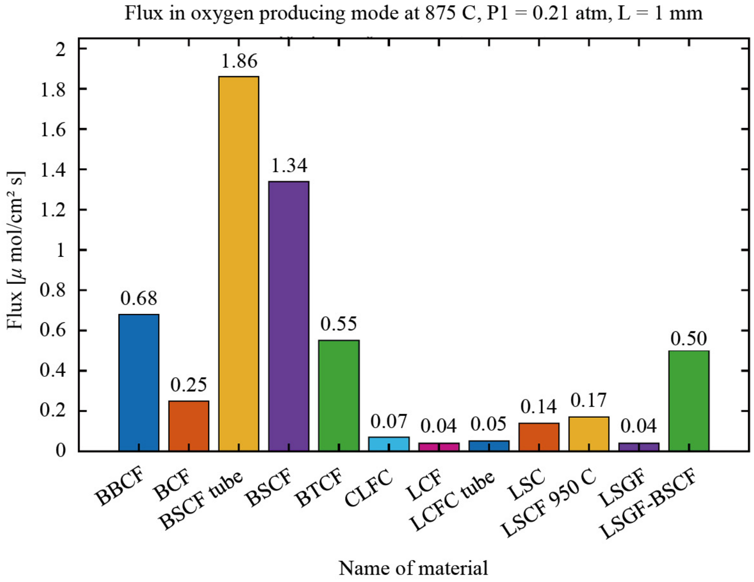

Figure 1. Oxygen permeation flux for different materials (Foy and McGovern [2])

A very recent review paper by Liu et al. [13] has emphasized the importance of CFD for enabling the technology for wide industrial applications and the need for improving CFD models by validating them against experimental data; and integrating them with emerging methods including, artificial intelligence, machine learning, and optimization. He indicated that, CFD tools are capable of exposing the complexities of the transport phenomena inside the Mixed Ionic–Electronic Conducting (MIEC) or Ion Trasport Membrane (ITM) reactors that are impossible to observe otherwise; and that CFD tools are needed to help design more efficient ITM reactors. The paper points out to the fact that more powerful computational power is needed to carry out CFD simulation, especially in three (3) dimensions.

Based on the literature review including 2025 papers, there seem to be very little work on validating CFD models with experimental data, mainly due to the scarcity of experimental studies. In terms of the CFD modelling, very few studies carried out geometric optimization of the membrane shape. For example, if we take the case of a concentric tube reactor, which is a preferred geometry, is it better (from energy generation and stability) to have the oxygen permeation and the combustion in the inner tube or the annulus. Many researchers worked on the stagnation reactor because in has the potential to produce high oxygen permeation; however, it presents major practical challenges in practical industrial applications.

The main objective of this paper is to develop a more realistic CFD model by validating the developed CFD model against the latest available data set for the BSCF membranes, for oxygen production (non-reactive) and oxy-combustion (reactive) cases. This objective requires the investigation of the oxy-fuel combustion process in a button cell reactor. A second equally important object is to use the experimentally validated model for simulating combustion in an annular reactor that can be used in industrial applications and carry out a sensitivity study to maximize the oxygen permeation making the system more efficient. In terms of mathematical modelling, I have formulated the problem addressed in a rigorous way stating the model equations and boundary conditions. This is rarely done in previous papers. I have also stated the underlying assumptions for the model equations.

In the first part of the study, we will formulate the mathematical model for the mOTR, including the permeation of oxygen through an Ion Transport Membrane (ITM), the transport and reaction of different species needed for simulating oxyfuel-combustion, and the radiation model, which is important in high-temperature applications. In the second part of the manuscript, the model validation is presented against the latest fully accessible experimental data [14]. In the third part, we will investigate the application of the model on an annular mOTR, which can be used for practical industrial applications.

Table 1. Summary of different membrane models used in published works

Author	Year	Type	Model	Remarks
Xu and Thomson [4]	1999	1-D (LSCF)	$J_{O_2} = \dfrac{D_V k_r \left(P'^{0.5}_{O_2} - P''^{0.5}_{O_2}\right)}{2Lk_f \left(P'_{O_2} P''_{O_2}\right)^{0.5} + D_V \left(P'^{0.5}_{O_2} + P'^{0.5}_{O_2}\right)}$ $D_V = D_V^o \exp\left[-\dfrac{E_D}{RT}\right]$ $D_V^o = 1.58 \times 10^{-2}\ \mathrm{cm^2/s}$ $E_D = 73.6\ \mathrm{kJ/mol}$ $k_f = k_f^o \exp\left[-\dfrac{E_f}{RT}\right]$ $k_f^o = 5.90 \times 10^6\ \mathrm{cm/atm^{0.5} \cdot\ s}$ $E_f = 226.9\ \mathrm{kJ/mol}$ $k_r = k_r^o \exp\left[-\dfrac{E_r}{RT}\right]$ $k_r^o = 2.07 \times 10^4\ \mathrm{mol/cm^2 \cdot\ s}$ $E_r = 241.3\ \mathrm{kJ/mol}$	Surface morphology of the membrane is dependent on the synthesis process and hence, k_r may vary by a factor α. As temperature increases, the surface exchange rate increases faster than the diffusion rate, until the process becomes diffusion-limited (from 750 °C to 950 °C).
Qi et al. [6]	2000	LSCF	$J_{O_2} = \frac{RT\sigma_i^o}{8F^2L}\ (P''^{-n}_{O_2} - P'^{-n}_{O_2})$	Oxygen vacancy diffusion is limited. Constants are determined by regression of the experimental data.
Yang and Lin [7]	2002	LSCF, SrCoFeO, LaSrCoO, SrCeFeO	$J_{O_{2-}} = \frac{3FD_V}{LV_m n}\ \ln\left[\frac{1+KP'^{n}_{O_2}}{1+KP''^{-n}_{O_2}}\right]$	Oxygen vacancy diffusion is limited. Several simplified assumptions are used in the point defect model. Experiments were conducted at various temperatures and pressures, and all the constants were regressed from the data.
Wang et al. [8]	2002	BSCFO	$J_{O_2} = \frac{\pi LC_i D_a}{2S\ ln(r_1/r_2)}\ ln\left[\frac{P'_{O_2}}{P''_{O_2}}\right]$	A temperature range of 700-900 °C was employed for the experiments, and the constants were regressed for the data.
van Hassel [9]	2004	Generic	$J_{O_2} = -\frac{\varepsilon}{\tau}\ x\left[\frac{1}{\frac{1}{D_{Kn,\,O_2}} + \frac{1-x_{02}}{D_{molO_2,\,N_2}}}\right]\left[\frac{P_{air}}{R_g T}\right]\left[\frac{1}{t_{pa}}\right]\left[\frac{dx_{O_2}}{dx}\right]$	Very detailed model
Liu and Gavalas [10]	2005	1-D (BSCF)	$J_{O_2} = Ak(T)G\left[(P'_{O_2})^n - (P''_{O_2})^n\right],\ n < 1$	No attempt was made to fit the experimental data with this model.
Tan et al. [11]	2007	LSCF	$F_{O_2} = \frac{0.79F_{Air}x\acute{_{O_2}}}{1-x\acute{_{O_2}}}$	
Mancini and Mitsos [12]	2011	2-D (LSCF & LNO)	$J_{O_2} = A\exp\left(-\frac{B}{T_M}\right)\left[\left(P'_{O_2}\right)^n - \left(P''_{O_2}\right)^n\right]$ LSCF LNO n 0.5 0.25 $A\ [\mathrm{mol \cdot m^{-2} s^{-1} Pa^{-n}}]$ 26.75 2.011 B [K] 16,510 10,240	A compromise between extremely detailed oxygen transport models and simplified black box models. The preexponential A accounts mostly for the diffusion coefficient and the membrane thickness dependence. B represents the effective activation energy or Arrhenius dependence due to both surface exchange kinetics and diffusion coefficient activation energy. Limited to a specific membrane thickness. It can't be extrapolated too far from the experimental condition.
Behrouzifar et al. [5]	2012	BSCFO	$J_{O_2} = \dfrac{\left[\frac{k_r}{k_f}\right]\left[\frac{1}{P''^{n}_{O_2}} - \frac{1}{P'^{n}_{O_2}}\right]}{\left[\frac{1}{k_f\ P'^{n}_{O_2}}\right] + \left[\frac{2L}{DV}\right] + \left[\frac{1}{k_f\ P''^{n}_{O_2}}\right]}$	Considers an elementary order for oxygen vacancy concentration and a non-elementary order for oxygen partial pressure

2. Description of the mOTR

Two reactors will be considered in this study. The first mOTR type is the button cell reactor, which has been used to conduct oxygen separation as well as oxyfuel combustion experiments in a few studies [14, 15], as shown in Figure 2a. The details of this setup will be given later in the experimental section. The second type is the annular mOTR shown in Figure 2b. In the shown configuration, air flows inside a circular tube, and oxygen permeates to the outer annulus. Fuel and carbon dioxide mixture flows in the annular section, where the permeated oxygen reacts with the fuel. In this case, the fuel chosen is methane (CH_4).

In a previous paper [16], we presented the features of a mini-ion-Transport Separator (mOTS) for oxygen separation, only for oxygen production. In that study, no combustion process took place. In this present study, we will investigate the oxy-fuel combustion in the mini-Oxygen Transport Reactor (mOTR), which has a 6 mm inner-tube diameter (D_i) and a 12 mm outer-tube diameter (D_o) and as shown in Figure 3. The length of the mOTR is taken as $L = 90$ mm. These dimensions are comparable to those of the experimental setup of Wang et al. [8].

In previous studies, simulations of fuel mixing with an OTR of similar size (Farooqui et al. [18]) were performed without (Farooqui et al. [18]) and with combustion (Ben-Mansour et al. [17]; Farooqui et al. [18]) inside the inner tube. In that previous study, the membrane model was not validated against experimental oxy-combustion data inside OTRs. The present model used in this investigation is more detailed, can model thick and thin membranes, and most importantly, has been validated against experimental oxygen separation and oxy-combustion data presented by Mezghani and Hamza [14].

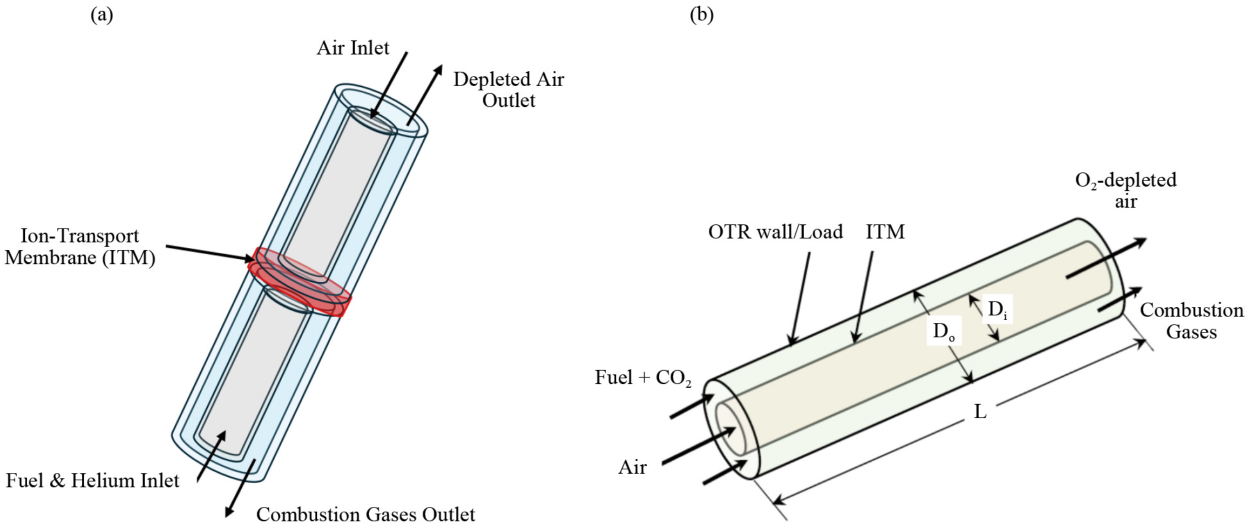

Figure 2. (a) Schematic of Button-cell mini-Oxygen Transport Reactor and (b) Schematic of annular mini-Oxygen Transport Reactor (mOTR)

Four different configurations of the mOTR are possible as shown in Figure 3: (1) air flowing in the inner tube and sweeping gas/fuel flowing in the annulus in parallel flow mode, (2) air flowing in the annulus and sweeping gas/fuel flowing in the tube in parallel flow mode, (3) configuration (1) with counter flow mode, and (4) configuration (2) with counter flow mode. All configurations can be practically implemented. Configurations (1) and (3) may offer easy cleaning of soot/carbon deposits of the tubes (from outside) if in-situ oxy-fuel combustion takes place. However, it is not difficult to design a cleaning method to clean the tubes from the inside.

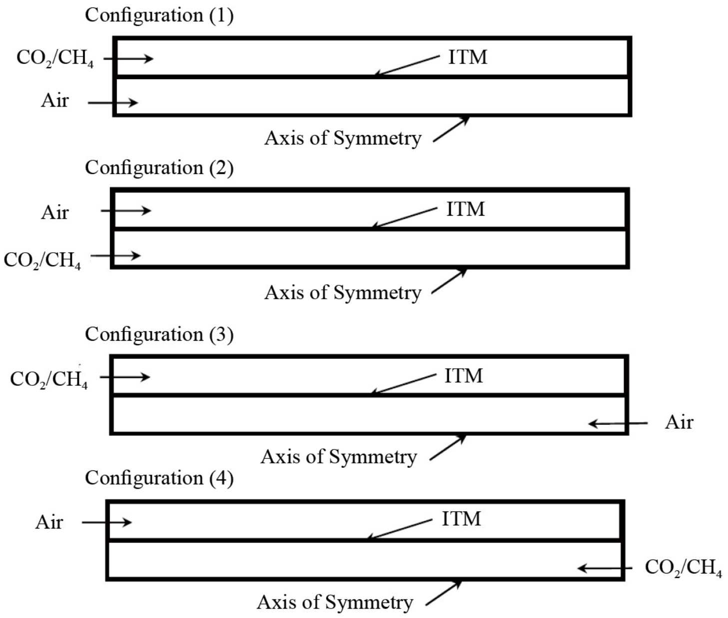

Figure 3. Axis-symmetric computational domain of mOTS/mOTR with four flow configurations

In this paper, we present the oxygen combustion cases for the first two configurations. Results will include oxygen fluxes as a function of air flow rates and sweeping gas (CO_2) flow rates. Taking advantage of axis-symmetry, we solve the problem only in a 2D axis-symmetric coordinate system.

3. Mathematical modeling and problem formulation

3.1 *General transport equations*

The transport phenomena in an Oxygen Transport Reactor (OTR) can be simulated by solving the necessary transport equation for both cases of oxygen separation and oxygen combustion. The model equations include mass, momentum, energy, and species conservation inside the OTR. The OTR is split into two compartments by the Ion Transport Membrane (ITM) (see Figures 2 and 3). The first compartment is the feed side, where air is fed at a given flow rate or average velocity, and the second compartment is the permeate side or sweep side, where, in the separation case, an inert gas (in this case, CO_2) is fed to enhance the oxygen separation. In the case of combustion, fuel is introduced with or without a sweeping gas.

Under steady state operations and with a laminar flow regime across both sides of the OTR, the mass, momentum, energy, and species equations can be written as follows.

The Mass-Species Conservation equation [19]

$$\nabla \cdot (\rho U) = S_i \tag{1}$$

Describes the conservation of different species. Since we are solving a multi-species problem, there is a source term for each species. A given species *i* can be consumed or produced due to combustion (chemical reaction) as described below in section 3.2.

The Momentum Conservation [20]

$$\nabla \cdot (\rho U U) = -\nabla p + \mu \nabla^2 U + S_m \tag{2}$$

is the momentum equation in all coordinate directions, written in vector form. It includes the momentum advection (transport by the flow motion), pressure gradient, and viscous terms. S_m is the momentum source term that may arise due to buoyancy or other forces.

The Energy Conservation ([21])

$$(\rho C_p)_f U \cdot \nabla T = \nabla \left(k_{eff} \nabla T\right) + S_e \tag{3}$$

Describes the thermal energy transport in the computational domain and includes the advection of thermal energy, the conduction term, and source terms S_e arising from radiative transport and fuel combustion.

The Species Conservation [19]

$$\nabla \cdot (\rho U Y_i) - \nabla \cdot (\rho D_{i,m} \nabla Y_i) = S_i \tag{4}$$

describes the transport of different gas species, including advection, diffusion, and a source term for each species that can arise from combustion (chemical reaction) as described in section 3.2.

Radiative heat transfer is important, especially in the case of combustion, and assuming no scattering and a constant absorption coefficient, the radiative transfer equation can be formulated as Siegel and Howell [22]:

$$\nabla \cdot I(\vec{r}, \vec{s}) = \kappa \left[\frac{\sigma T^4}{\pi} - I(\vec{r}, \vec{s})\right] \tag{5}$$

The detailed derivation of Eq. (5) is given in standard Thermal Radiation Heat Transfer books such as Siegel and Howell [22]. The left-hand-side term refers to the change of radiative intensity I as a function of position $\overrightarrow{r}$ in the direction of the intensity ray $\overrightarrow{s}$. This change in intensity is due to the emission by the media (a positive contribution) and absorption by the media (a negative contribution).

For the oxygen separation only (non-reactive cases), the whole reactor is set at a constant temperature. Therefore, radiative heat transfer is zero since the reactor is isothermal. For the reactive cases, radiative transfer is important and neglecting it can lead to large errors in the predicted temperature field. This error can be of the order of a few hundred kelvin in ITM reactors. In this case, the gases constitute a participating medium since carbon dioxide and water vapor are radiatively participating gases. We have used the Weighted Sum of Gray Gases (WSGG) known give good accuracy with reasonable computational effort [23]. The model has been tried for realistic oxyfuel combustion CFD calculations and has given accurate results [24].

Finally, the membrane model is needed to predict the local oxygen permeation at any point along the permeate side of the membrane. The oxygen permeation-ITM based on the recently developed rearranged model of Behrouzifar et al. [5]:

$$J_{O_2} = \frac{D_v k_r \left[(P_1)^{0.25} - (P_2)^{0.25}\right]}{2L_m k_f (P_1)^{0.25} (P_2)^{0.25} + ((P_1)^{0.25} + (P_2)^{0.25}) D_v} \tag{6}$$

Equation (6) represents a membrane model and is derived in detail by Behrouzifar et al. [5]. Membrane models have been summarized in Table 1. The models are semi-empirical models. The general form of the model are derived based on the transport balance of the oxygen transport through an Inon Transport Membrane. The main transport mechanisms include the disassociation of the oxygen molecule into two oxygen ions and two electrons, followed by the adsorption of oxygen ions, diffusion of the oxygen ions, and the desorption and recombination of ions with electrons. The detailed derivation is given in the paper by Xu and Thompson [4]. The model constants (D_v, k_r, k_f) are material dependent and need to be determined experimentally; and L_m is the membrane thickness. In essence, Equation (6) states that the oxygen permeation flux through the membrane is driven by the difference in partial pressure of oxygen and material transport properties.

To complete the mathematical model formulation, it is important to specify all the boundary conditions (B.C.). These need to be given for all equations (flow, heat transfer, and mass transfer).

For the flow Equations (1) and (2):

At the inlet (see Figure 3), $x = 0$, $V = V_{\text{in}}$ (Velocity B.C.);

At the outlet $x = L$, $p = p_{\text{atm}}$ (Atmospheric pressure B.C.);

At the wall of reactor $y = y_2$, $u = v = 0$ (No slip B.C.);

At the axis $y = y_1$; $\frac{\partial u}{\partial y} = \frac{\partial v}{\partial y} = 0$ (Symmetric flow B.C.).

For the energy (Heat Transfer) Equation (3):

At the inlet $x = 0$, $T = T_{\text{in}}$ (Gas mixture inlet temperature);

At the outlet $x = L$, T_{out} (Backflow temperature);

At the wall of reactor $y = y_2$, $T = T_{\text{wall}}$ (Wall Temperature);

At the axis $y = 0$, $\frac{\partial T}{\partial y} = 0$ (Symmetry B.C.).

For the species Equation (4), the mass fraction of the different gas species: oxygen, nitrogen, methane, and carbon dioxide, is prescribed according to the configuration treated:

At the inlet $x = 0$, $Y_i = Y_{i,\text{ in}}$ for all species (Inlet mass fractions);

At the outlet $x = L$, $Y_{i,\text{ out}}$ (Backflow mass fractions);

At the wall of reactor $y = y_2$, $Y_i = 0$ (Wall Temperature);

At the axis $y = 0$, $\frac{\partial Y_i}{\partial y} = 0$ (Symmetry B.C.).

For the radiative equation we need to define the emissivity at all the wall, inlets and outlet which were all set to a realistic value of $\varepsilon = 0.8$. One the temperature boundary conditions are set, the radiative intensity boundary conditions will be automatically computed.

3.2 *Reaction mechanisms for oxy-fuel combustion*

The application of CFD in combustion-related studies is usually computationally demanding [25]. This necessitates the use of reaction mechanisms that are simplified to minimize the computing tasks. Despite the recent use of detailed reaction mechanisms in combustion as a result of the current upsurge in computational capabilities and more accuracy, the reduced or global mechanisms are still preferred due to economic considerations [26]. It is widely accepted that, in order to simulate complex geometries as well as chemical reactions involving several species, simplified chemical kinetic mechanisms are essential. Among the well-known reduced schemes for methane-air/oxy combustions are the global single-step reaction model, the two-step Westbrook and Dryer (WD) model, and the modified Westbrook and Dryer for oxy-fuel combustion. Reaction I shows the single-step oxidation mechanism of methane, which is available in ANSYS Fluent:

$$CH_4 + 2O_2 \rightarrow CO_2 + 2H_2O \quad \text{[Reaction I]}.$$

The two-step chemical kinetic reactions developed by Westbrook and Dryer [27], which are available as a default in the ANSYS Fluent code, are presented in Reactions II-VI. The model was modified by Yin et al. [28] to handle the increased CO_2 concentration under oxy-fuel conditions. The Westbrook and Dryer mechanism consists of two reactions, with the last reaction being reversible. The mechanism is listed in the form of three irreversible steps as follows:

$$CH_4 + 1.5O_2 \rightarrow CO + 2H_2O \quad \text{[Reaction II]},$$

$$CO + 0.5O_2 \rightarrow CO_2 \quad [\text{Reaction III}],$$

$$CO_2 \rightarrow CO + 0.5O_2 \quad [\text{Reaction IV}].$$

Table 2 shows the kinetic rate data for the three reaction mechanisms: (a) Single-step, (b) Original WD, and (c) Modified WD. In the modified WD reaction mechanism for oxy-fuel conditions, the first chemical kinetic mechanism of CH_4 and O_2 reaction in the WD model was retained, while refining the second CO-CO_2 reactions to improve the computation of the concentrations of the CO and CO_2 species.

Table 2. List of notations for the optimization problem

	(a) The original WD reduced mechanism			
Reaction	Rate of Reaction [kmol/(m³s)]	A	b	E
$CH_4 + 2O_2 \rightarrow CO_2 + 2H_2O$	$\frac{d[CH_4]}{dt} = AT^b e^{-\frac{E}{RT}} \cdot [CH_4]^{0.7}[O_2]^{0.8}$	2.119E11	0	2.027E08
	(b) The original WD reduced mechanism with kinetic rate data			
$CH_4 + 1.5O_2 \rightarrow CO + 2H_2O$	$\frac{d[CH_4]}{dt} = AT^b e^{-\frac{E}{RT}} \cdot [CH_4]^{0.7}[O_2]^{0.8}$	5.012E11	0	2.0E08
$CO + 0.5O_2 \rightarrow CO_2$	$\frac{d[CO]}{dt} = AT^b e^{-\frac{E}{RT}} \cdot [O_2]^{0.25}[CO][H_2O]^{0.5}$	2.239E12	0	1.7E08
$CO_2 \rightarrow CO + 0.5O_2$	$\frac{d[CO_2]}{dt} = AT^b e^{-\frac{E}{RT}} \cdot [CO_2]$	5.000E08	0	1.7E08
	(c) The modified Westbrook-Dryer mechanism for oxyfuel reaction			
$CH_4 + 1.5O_2 \rightarrow CO + 2H_2O$	$\frac{d[CH_4]}{dt} = AT^b e^{-\frac{E}{RT}} \cdot [CH_4]^{0.7}[O_2]^{0.8}$	5.012E11	0	2.0E08
$CO + 0.5O_2 \rightarrow CO_2$	$\frac{d[CO]}{dt} = AT^b e^{-\frac{E}{RT}} \cdot [O_2]^{0.25}[CO][H_2O]^{0.5}$	2.24E06	0	4.18E07
$CO_2 \rightarrow CO + 0.5O_2$	$\frac{d[CO_2]}{dt} = AT^b e^{-\frac{E}{RT}} \cdot [CO_2][O_2]^{-0.25}[H_2O]^{0.5}$	1.10E13	-0.97	3.28E08

4. Model implementation and validation

4.1 *Method of Solution and Computational Implementation*

Equations (1) to (6), along with the boundary conditions, define the mathematical model for the problem at hand. Equations (1) to (4) are partial differential equations that define conservation of mass, momentum, energy, and species. The source term for the species equation is obtained by the actual chemical reactions and the reaction coefficients involved. The source terms for the energy equation come from the heat generated by the chemical reaction and the different modes of heat transfer taking place in the reactors. Since we are dealing with temperatures that can reach 1,500 K, thermal radiation is very important and needs to be accounted for to predict the correct temperature in the reactors and hence the correct heat transfer rates. Equation (5) is the Radiative Transfer Equation (RTE). This is a highly nonlinear partial differential equation and can become an integral-differential equation if scattering occurs in the reactor. Equation 6 defines the oxygen transport across the Ion Transport Membrane.

As described above, we are dealing with the solution of a very complex system of nonlinear partial differential equations, including the Navier-Stokes and the radiative transfer equations, coupled with complex chemical reactions. These equations can only be solved using numerical techniques. In our study, we use the finite volume method to discretize the set of Partial Differential Equations (PDEs) (1) to (5). The main challenges of the numerical/computational algorithm are listed below:

- Non-linearity of the Navier-Stokes equations
- The numerical solution is needed in two domains separated by the membrane (the feed or air side and the permeation or combustion side, as indicated in the Figures 1-3 above).
- Complexity of the chemical reaction mechanisms, coupled with the combustion process and species transport
- The highly nonlinear nature of the radiative transfer equations is needed to model gas radiation in the combustion space, where some of the gases, including carbon dioxide and water, participate in radiative heat transfer.

The above challenges are addressed as follows:

- The solution of the above coupled system is solved in an iterative manner
- Because of the nonlinear nature of the Navier-Stokes equation, the reaction mechanisms, and the radiative transfer, we under-relax the iterative algorithm to avoid divergence of the solution process.
- The solution is carried in steps: we start by solving the isothermal flow until the flow field is converged in both domains, then we enable the membrane model to allow oxygen transport across the membrane, later we invoke the energy equation coupled with chemical reaction and the combustion as well as the species transport, and the final step we invoke the solution of radiative transfer equation until convergence of the solution of all equations.

The above equations are discretized using the finite volume method [29] to ensure conservation is guaranteed at each iterative step. The mesh used is a structured mesh, and mesh independence has been done to ensure that the obtained solution is grid independent.

4.2 *Implementation of membrane models*

The finite volume formulation of the fluid flow, heat transfer, chemical reaction mechanisms, combustion process, chemical transport, and the radiative transfer model equations are implemented in the ANSYS Fluent Software [19], which has been used to solve these equations. However, the membrane model is not available, and an additional User-Defined Function (UDF) needs to be developed, compiled, and coupled with the main software to simulate the oxygen transport through the ion transport membrane.

4.3 *Validation for oxygen separation without combustion (non-reactive case)*

The mathematical model equations have been implemented in ANSYS Fluent CFD software. This software can solve the general transport equation. However, it does not have a membrane model. To implement the membrane model, a UDF had to be written and linked with Ansys Fluent Software. Before using the OTR developed model, we need to validate it against experimental data. Hence, the numerical results are validated against the experimental results of Behrouzifar et al. [5] as shown in Figure 4. A grid independence study has been done to ensure the results are mesh independent. The final adopted mesh is a uniform structured mesh with a cell size of 0.4 mm by 1 mm. Such a problem has a few challenges to keep in mind, including: (1) a compressible flow regime with variable properties, (2) radiation modelling must be included, (3) the computational domain contains two fluids, and (4) the membrane model has temperature nonlinearity in addition to the inherent nonlinearity of the Navier-Stokes equations. To obtain good convergence, low under-relaxation factors are applied to all equations.

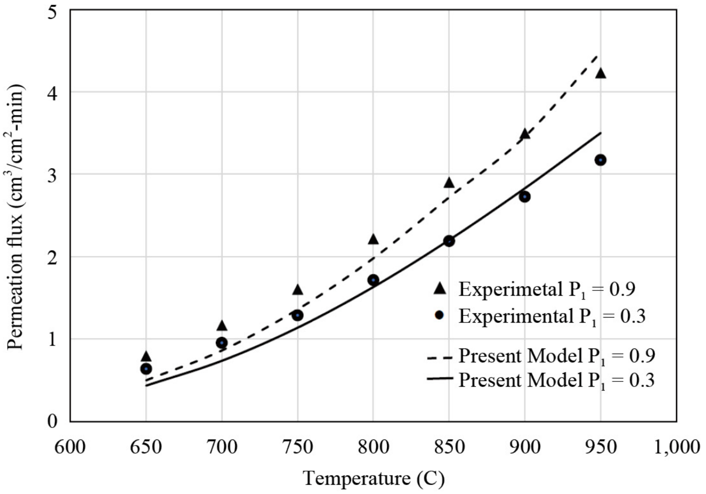

Figure 4. Membrane model validation for various temperatures and two oxygen partial pressure values (P_1 = 0.3 and P_1 = 0.9) against experimental data of Behrouzifar et al. [5]

4.4 *Validation for oxygen separation and combustion (reactive case)*

Experimental data for oxyfuel combustion are rare. The published data present cases only for the button-cell configuration, as shown in Figure 5. The operating conditions for the OTR are explained in detail in Mezghani and Hamza [14]. The major details of the experimental OTR have been matched in the computational simulation. The mesh for the computational study used for the validation of the model is presented in Figure 6.

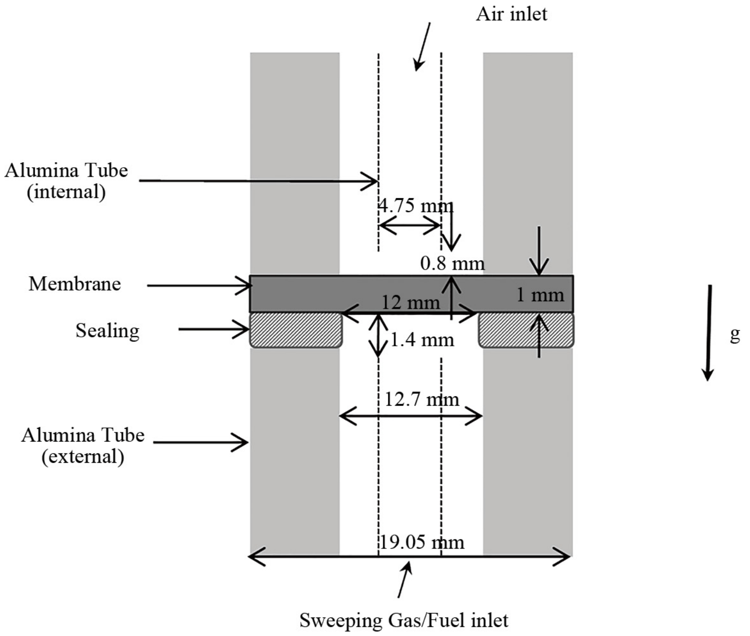

Figure 5. Schematic of the KFUPM experimental OTR setup

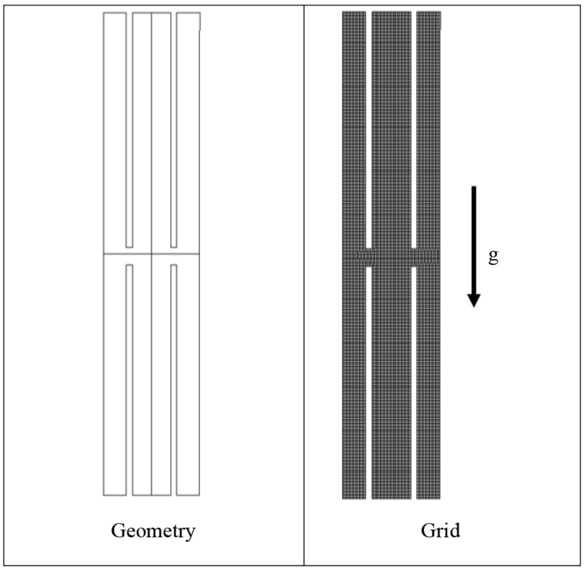

Figure 6. Computational geometry and the grid of OTR

In the experimental study, oxy-fuel combustion tests of the BSCF membranes were conducted. The OTR was operated with a mixture of helium and methane in the sweep side. The flow rate of helium (in the experimental setup) was constant (3 ml/min), whereas the methane flow rate was variable. The air-feed flow rate was kept constant at 34 ml/min. The experiments were conducted at 925 °C and atmospheric pressure. The permeate pressure was slightly higher than atmospheric by 3 to 6 mBar. For repeatability, each experimental data point represents an average value of three Gas Chromatography System runs with a maximum statistical error of 0.5%.

A gas chromatographer was used to analyse the gas composition after condensing the water vapor. The results are presented in Figure 7. It was observed that there are no measurable traces of CO gas; therefore, the first reaction was the most likely one. Accordingly, the oxygen flux is calculated based on the full conversion of methane to CO_2 and water.

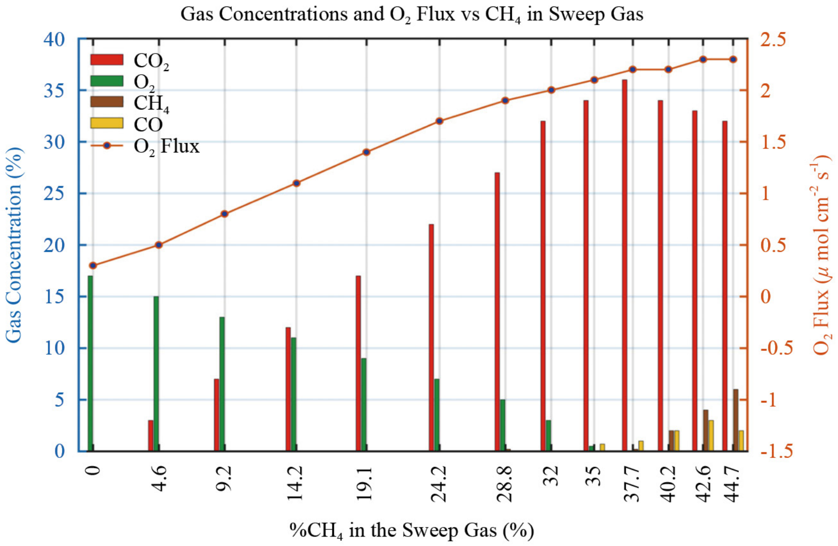

Figure 7. Experimental Gas analysis of the sweep gas after the combustion reaction and the oxygen permeability of BSCF membrane versus methane concentration (Mezghani and Hamza [14])

Based on the experimental results of Figure 7, the oxygen flux through the membrane increases with the increase in the methane concentration. This was expected as the fuel-oxygen combustion reduces the partial pressure of oxygen on the permeate side (combustion side), therefore creating a larger oxygen partial pressure difference, which has the potential for oxygen permeation through the membrane.

Experimental runs 3, 5, 9, 11, and 13 with % methane in the sweep stream shown in Figure 7 have been chosen arbitrarily for the validation of the CFD models described above. The operating conditions for these cases are given in Table 3.

Table 3. Operating parameters for the selected runs

% Methane	Methane flow rate (ml/min)	Helium flowrate (ml/min)	Air flowrate (ml/min)	OTR Temperature
9.2	0.304	3	34	925
19.1	0.708	3	34	925
35.0	1.615	3	34	925
40.2	2.017	3	34	925
44.7	2.425	3	34	925

The experimental oxygen permeation flux is presented in Figure 8. These cases were modelled using the original two-step WD mechanism and the modified WD, and the results are compared to the experimental data in Figure 8. The two models gave similar predictions of the oxygen permeation flux, and both showed good agreement with the experimental results except for the two extreme percentages of methane concentrations in the sweep side, where there were slight deviations - under-predicting at the lowest methane percentage of 9.2% and slightly over-predicting at 44.7% methane.

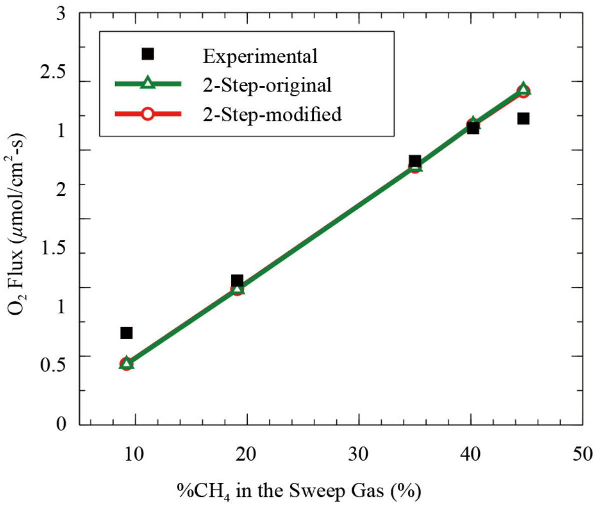

Figure 8. Oxygen permeation of BSCF membrane versus methane concentration in the sweep side

The increase in the methane concentration resulted in the overall increase in the sweep gas flow rate; thus, the higher sweep flow rate, the more the oxygen vacancies at the membrane surface, leading to an increase in the oxygen permeation. Also, an increase in methane concentration elevates the overall reaction heat released, which in turn increases the oxygen flux due to temperature elevations. Hence, the higher the methane concentration in the sweep gas, the more the oxygen permeation flux, as shown in Figure 8.

The large increase in oxygen flux under reactive flow, which can be as much as 4 to 6 times higher in comparison to non-reactive flow in a stagnation flow reactor, as reported experimentally by Kirchen et al. [15] for an LCFO membrane and Mezghani and Hamza [14] for a BSCF membrane. This increase is caused mainly by the drastic reduction in the partial pressure of oxygen on the permeate-reacting side. For full combustion, the partial pressure on the reactive side becomes almost zero, and hence, the only resistance to oxygen permeation is the feed side and the membrane.

This increase in oxygen permeation can be further augmented by the increase in temperature of the reactor and therefore, the membrane. This leads to higher diffusion of the oxygen ions through the membrane, as verified experimentally by many studies, including Xu and Thompson [4] and others. As reported by Behrouzifar et al. [5], the diffusion coefficient D_v and the surface adsorption/desorption coefficient k_f and k_r (in Equation 6) are functions of temperature. Experimental results have shown that an increase in the membrane temperature by 100 K will result in almost 100% increase in the oxygen flux. In our study, the temperature dependence of all these coefficients has been implemented in our CFD model through a User Defined Function (UDF) along with the Membrane model.

The experimental gas concentrations at the sweep side exhaust were compared with the numerical simulation results obtained using both the original WD model and the modified WD model, as shown in Figure 9. The original WD model and the WD modified model predicted the concentration of unburned methane well. For the carbon dioxide, the modified WD model gave better prediction at the higher CH_4 percentage in the sweep side.

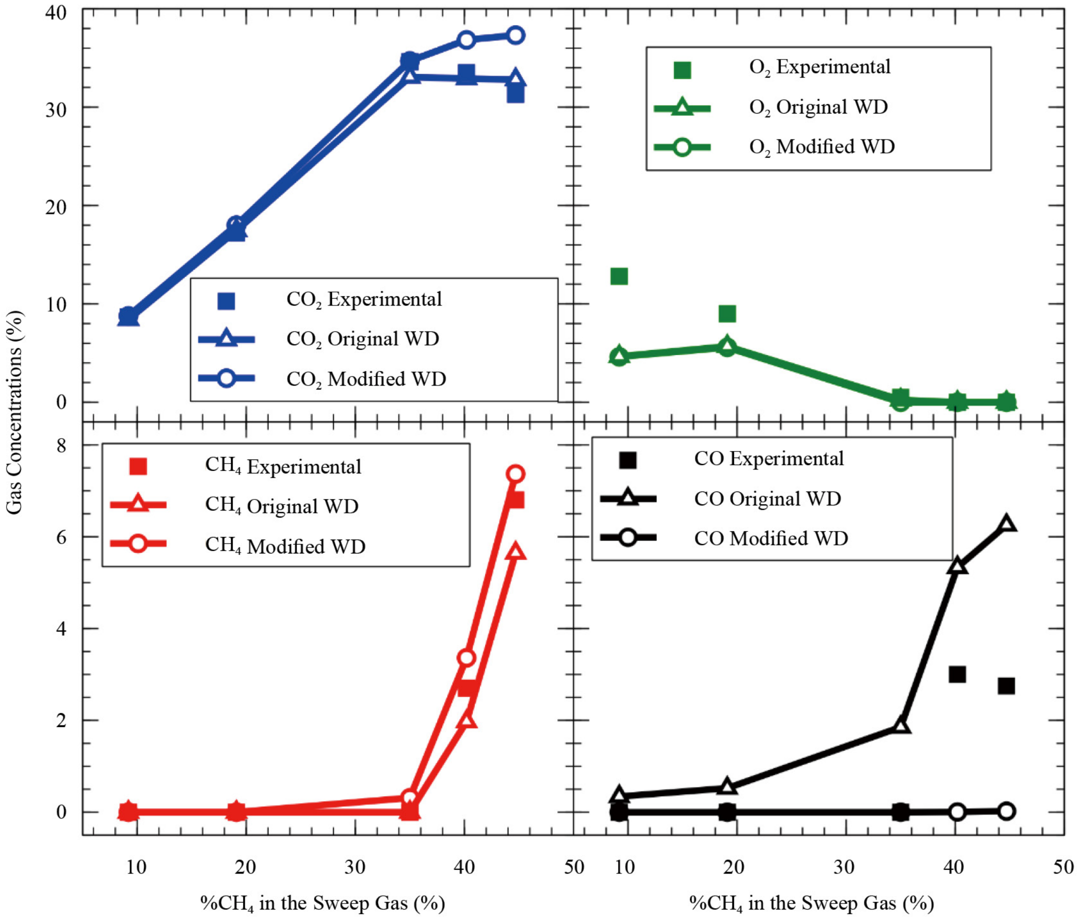

Figure 9. Comparison between experimental gas (CH_4, O_2, CO, CO_2) concentrations with the numerical simulation results at the sweep side exhaust

Looking at the oxygen concentrations (Figure 9), we can note that despite the slight overprediction of the excess oxygen at a lower percentage of methane in the sweep gas inlet, there was good agreement between the experimental results and the original WD model predictions at higher percentages of methane. Both models gave similar predictions of the O_2 concentrations.

Finally, the CO concentrations are predicted well at low methane percentage (below 20%). At high methane percentage (above 40%), both models fail to predict the CO concentration. The modified WD model gave good CO prediction for the medium methane percentage (around 30%).

This deviation can be caused by limitations in the reaction kinetic model, but it can also be due to the experimental method of collecting the gas concentration.

In the experiment by Mezghani and Hamza [14], they used a gas chromatography technique. This method takes 25 to 30 min to measure the gas concentration. It is possible that the delay may cause further reactions of some gases and therefore a change on the concentration at the exhaust of the reactor. On the other hand, the CFD predictions do not account for any delay or possible reactions outside the reactor.

The general trend of the CO_2 gas generation increases with the increase in methane percentage in the sweep gas up to about 35%, after which the generation slightly decreases due to the increase in unburned methane, as seen in Figure 9. The excess oxygen decreases with an increase in methane concentration in the sweep gas. The stoichiometric condition was found to occur around 35% methane, corresponding to the complete reaction of methane with oxygen. The CO concentration became significant beyond 35% methane in the sweep side due to excess fuel in the reactor.

We conclude the discussion of the comparison between the experimental results and predicted values by looking at the normalized difference between both. We have presented the normalized Root Mean Square (RMS) of the differences in Table 4 below. We have normalized the RMS values using two methods: first, with respect to the average values of both experimental and predicted values, and second, with respect to the maximum range of the data set (as normally done in instrumentation analysis).

Table 4. Normalized RMS of differences between experimental and predicted results

Data Description	Normalized w/r to average	Normalized w/r to maximum
Oxygen flux–non-reactive case (Figure 4, P_1 = 0.3)	5.13%	2.78%
Oxygen flux–non-reactive case (Figure 4, P_1 = 0.9)	6.27%	3.44%
Oxygen flux–reactive case (Figure 8, WD Model)	9.19%	6.13%
Oxygen flux–non-reactive case (Figure 8, Modified model)	8.55%	5.58%

For further understanding of the flow, temperature, and species fields under oxy-combustion process with methane, these fields are presented for the case of experimental run 5 with 19.1% methane in the sweep stream as obtained from the three reaction models: Single-step, Original WD, and Modified WD, as described earlier. The computational field and numerical mesh used for the CFD simulations were shown earlier in Figure 6. The flow velocity field is shown in Figure 10. The velocity field vectors and the velocity magnitudes were similar for all three models employed, as shown in Figure 10, respectively.

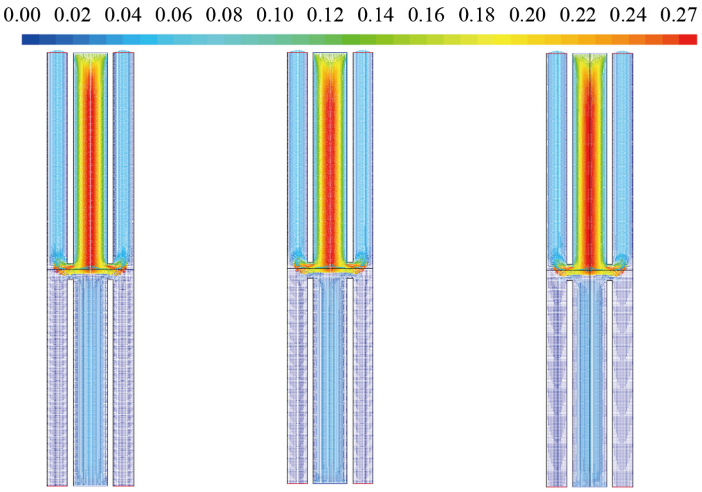

(i) Single Step (ii) Original WD (2-step) (iii) Modified WD (2-step)

Figure 10. Velocity field vectors coloured by velocity magnitude in the OTR for case [m/s]

In all cases, the velocity magnitude (Figure 11) was higher at the center of the inner pipes for both feed and sweep sides, and much higher at the feed side due to the higher flow rate of 34 l/min as compared to the sweep side.

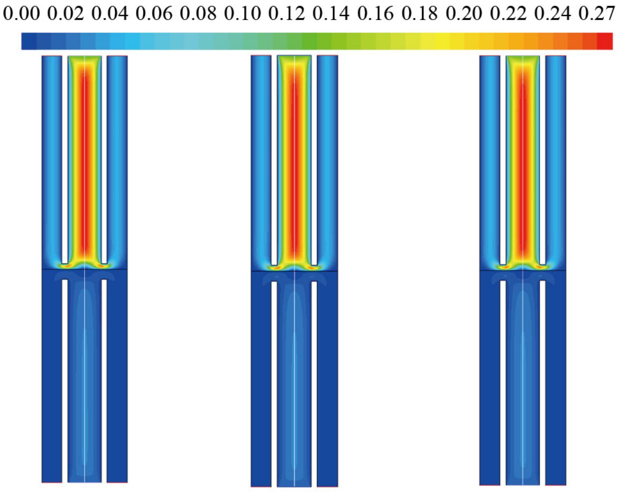

(ii) Single Step (ii) Original WD (2-step) (iv) Modified WD (2-step)

Figure 11. Velocity magnitude contours in the OTR [m/s]

The temperature contours presented in Figure 12 for the three models show the region near the membrane surface depicting the methane oxidation zone. The two-step models predicted much higher maximum temperatures in the combustor compared to the single-step model, as shown in Figure 12, but there was not much obvious difference among the two-step models.

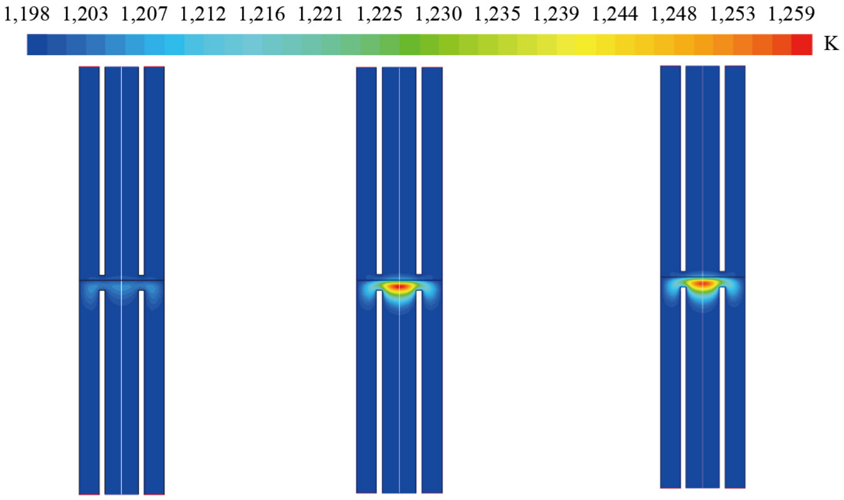

(iii) Single Step (ii) Original WD (2-step) (v) Modified WD (2-step)

Figure 12. Temperature contours in the OTR

The oxygen mole fraction contours are shown in Figure 13. Also, the two-step models predicted similar mole fractions in the sweep side, but slightly higher than the single-step prediction. (HOW)

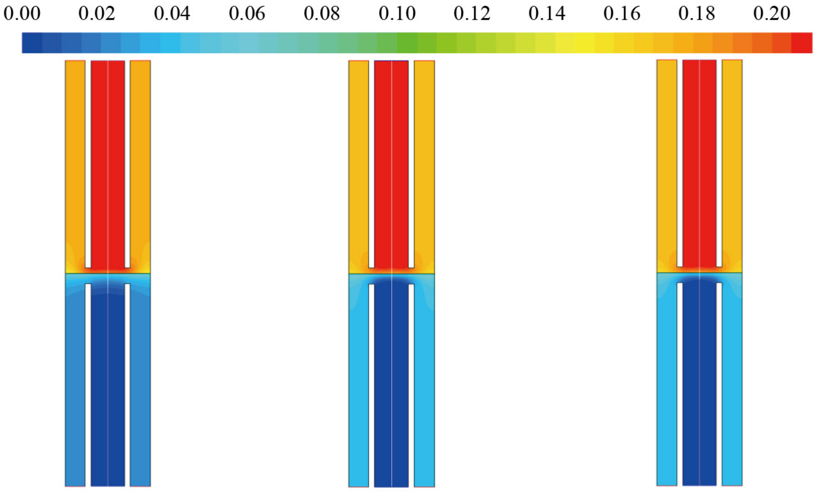

(iv) Single Step (ii) Original WD (2-step) (vi) Modified WD (2-step)

Figure 13. Mole fraction contours of O_2

As for the contours of CO_2, there was no significant difference among the three models, as shown in Figure 14. The CO_2 was produced from the reaction zone near the membrane surface in the sweep side and attained its maximum fraction downstream on the sweep side. The CO was predicted only by the two-step models since the single-step reaction does not account for CO production.

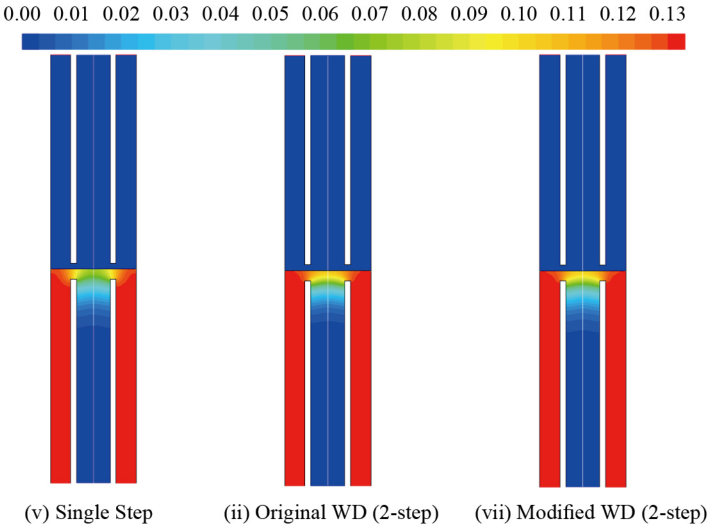

(v) Single Step (ii) Original WD (2-step) (vii) Modified WD (2-step)

Figure 14. Mole fraction contours of CO_2

The contours of the CO shown in Figure 15 indicate that the original WD model predicted higher CO in the reaction zone and significant CO emitted out of the sweep side. The CO produced using the modified WD model was consumed within the reaction zone near the membrane surface, and hence less CO in the exhaust. The methane mole fraction contours shown in Figure 16 are similar for all three models' predictions. The methane was totally consumed near the membrane surface in all the models, and hence there were no unburnt methane traces at the exhaust of the sweep side. The H_2O mole fraction contours were also similar for all three models, with production starting from the reaction zone near the membrane surface in the sweep side and attaining maximum fraction downstream the sweep side.

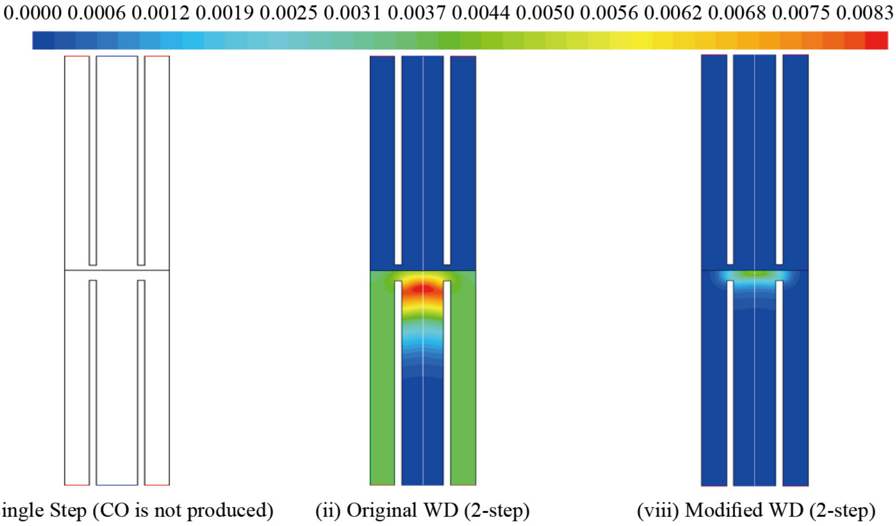

(vi) Single Step (CO is not produced) (ii) Original WD (2-step) (viii) Modified WD (2-step)

Figure 15. Mole fraction contours of CO

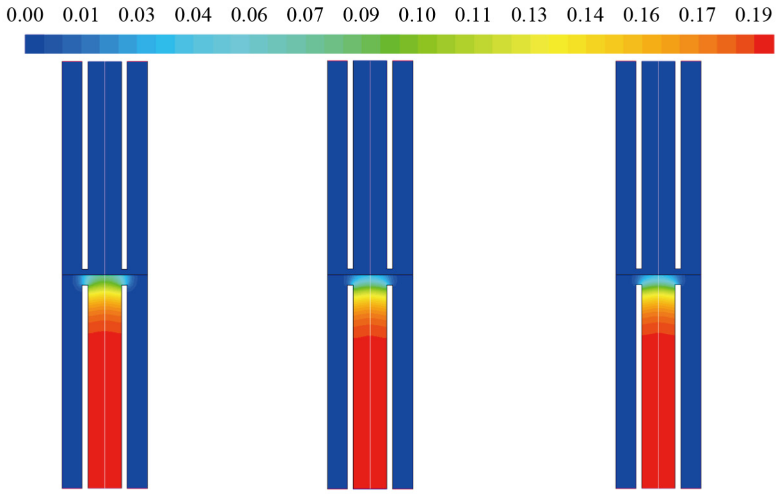

(vii) Single Step (ii) Original WD (2-step) (ix) Modified WD (2-step)

Figure 16. Mole fraction contours of CH_4

5. Results and discussion for the annular system

5.1 *Oxygen separation results for annular mOTS*

Table 5. Summary of parametric study for oxygen separation in configuration 1 (Air flows inside tube)

Case #	Average Air velocity $\overline{V}_{air}$ (m/s)	Average CO_2 velocity $\overline{V}_{CO_2}$ (m/s)	O_2 flow rate permeated $\dot{m}_{O_2}$ (kg/s)	Pressure Drop in the Air Side ΔP_{air} (Pa)	Pressure Drop on the CO_2 side ΔP_{CO_2} (Pa)
1	0.05	0.05	8.845×10^{-8}	0.149	0.271
2	0.1	0.05	1.369×10^{-7}	0.321	0.280
3	0.2	0.05	1.990×10^{-7}	0.684	0.289
4	0.3	0.05	2.347×10^{-7}	1.060	0.294
5	0.4	0.05	2.570×10^{-7}	1.444	0.297
7	1.0	0.05	3.054×10^{-7}	3.851	0.303
9	2.0	0.05	3.253×10^{-7}	8.187	0.306
11	1.0	0.1	4.619×10^{-7}	3.795	0.578
12	1.0	0.2	6.317×10^{-7}	3.738	1.111
13	1.0	0.3	7.246×10^{-7}	3.707	1.640
14	1.0	0.5	8.276×10^{-7}	3.672	2.698
15	1.0	1.0	9.417×10^{-7}	3.629	5.384
16	1.0	1.5	1.000×10^{-6}	3.604	8.144
17	1.0	2.0	1.041×10^{-6}	3.586	10.98
18	1.0	2.5	1.072×10^{-6}	3.572	13.89

The full details of oxygen separation studies have already been published by the author Ben-Mansour [16]. In this section, we summarize the main results of the oxygen separator in the annular system. In our simulation studies, we extended the range of flow velocities from 0.05 m/s to 2.5 m/s. The lower limit is typical of velocities in most experimental setups, including King Fahd University for Petroleum and Minerals (KFUPM), experiment. The upper limit is chosen to keep erosion at a minimum. Though higher velocity operation may offer a self-cleaning mechanism and offer high flux permeation, it can cause high rates of erosion to composite ITM membranes. Overall, the flow in all cases is laminar with a Reynolds number below 100. The simulated cases for oxygen separation for configurations (1) and (2) are summarized in Tables 5 and 6, respectively. More than 30 cases have been simulated to investigate the effect of the air velocity, sweeping fluid (CO_2) velocity on separation for both geometric configurations (1) and (2). In all the cases, no fuel was introduced with the sweeping gas CO_2. To obtain high-accuracy prediction, a double-precision solver has been used on a 64-bit workstation. In addition, the relative residual of the mass momentum, species, and energy equation were taken to be 1e-11 to ensure fully converged solutions.

Table 6. Summary of parametric study for oxygen separation in configuration (2) (Air flows inside annulus)

Case #	Average Air velocity $\overline{V}_{air}$ (m/s)	Average CO_2 velocity $\overline{V}_{CO_2}$ (m/s)	O_2 flow rate permeated $\dot{m}_{O_2}$ (kg/s)	Pressure Drop in the Air Side ΔP_{air} (Pa)	Pressure Drop on the CO_2 side ΔP_{CO_2} (Pa)
20	0.05	0.05	1.009×10^{-7}	0.254	0.216
21	0.1	0.05	1.163×10^{-7}	0.527	0.221
22	0.2	0.05	1.269×10^{-7}	1.079	0.224
23	0.3	0.05	1.310×10^{-7}	1.633	0.226
24	0.5	0.05	1.345×10^{-7}	2.750	0.227
25	1.0	0.05	1.370×10^{-7}	5.578	0.227
26	2.0	0.05	1.382×10^{-7}	11.39	0.228
27	1.0	0.1	2.384×10^{-7}	5.560	0.437
28	1.0	0.2	3.940×10^{-7}	5.535	0.844
29	1.0	0.3	5.026×10^{-7}	5.519	1.245
30	1.0	0.5	6.468×10^{-7}	5.498	2.051
31	1.0	1.0	8.434×10^{-7}	5.469	4.144
32	1.0	1.5	9.599×10^{-7}	5.451	6.375
33	1.0	2.0	1.046×10^{-6}	5.437	8.751
34	1.0	2.5	1.115×10^{-6}	5.426	11.27

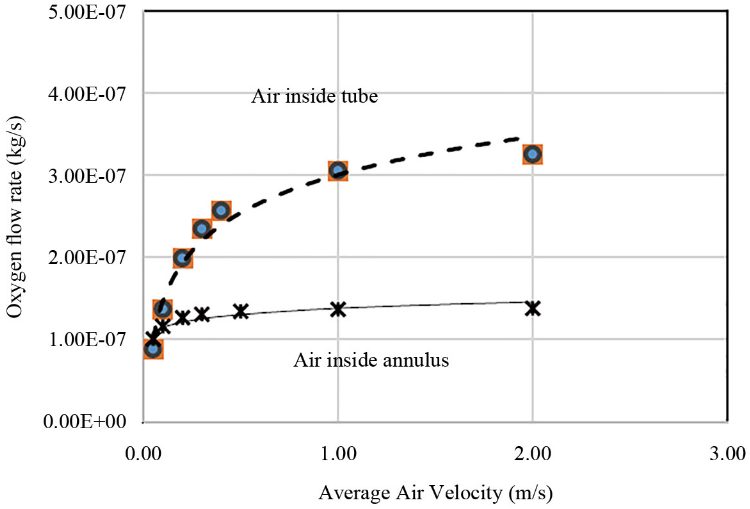

Figure 17. Effect of air velocity on permeated oxygen for sweep velocity of 0.05 m/s for configurations (1) and (2) as shown in Figure 3

The most important output from the mOTS is the amount of separated/permeated oxygen across the ITM. First, we look at the effect of average air velocity on the oxygen mass flow rate. The oxygen mass flow rate for the system is plotted against the air velocity for both configurations (1) and (2) and presented in Figure 17. It is noted that placing air inside the tube can give much better separation than placing the air in the annulus. This is a novel finding that has been discovered in the study. This result indicates that placing air inside the tube not only offers better system cleaning if we were to use the system as a reactor but also offers almost 2.5 times the permeated oxygen when operating the system as an oxygen separator.

5.1.1 *Effect of sweeping gas (CO_2) velocity*

The permeated oxygen flow rate as a function of sweeping gas velocity is shown in Figure 18. For this part of the investigation, the air velocity is fixed at 1.0 m/s. The permeated oxygen flow rate data in both configurations are fitted with a Logarithmic trendline. The data indicate that varying the sweep gas has a much stronger effect on enhancing oxygen permeation across the ITM. This is due to the sweeping gas, which reduces the partial pressure of oxygen to very low values. The higher the velocity, the more effective the sweeping results in larger permeation. We further note that both configurations (1 and 2) result in almost the same permeation of O_2 at the upper limit (due to erosion), sweeping velocity of 2.5 m/s.

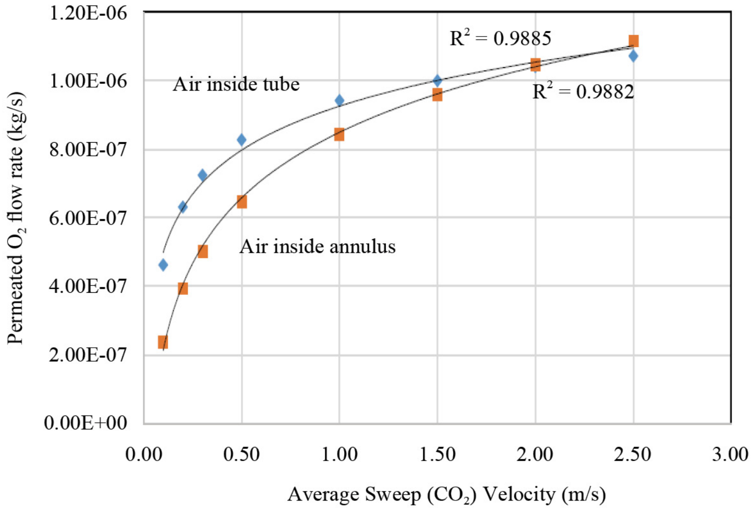

Figure 18. Effect of sweep gas velocity on permeated oxygen for an air velocity of 1m/s for configurations (1) and (2) (as shown in Figure 3)

5.2 *Oxy-combustion results in annular reactor*

5.2.1 *Combustion in the annulus side (air inside the tube)*

The same geometry has been adopted for the oxy-combustion cases, which have been simulated using a single-step reaction, assuming diffusion flame combustion.

The following oxy-fuel combustion cases have been simulated for the case where the combustion takes place in the annulus. They are listed in Table 7. We will refer to these cases as annular oxy-combustion cases.

From the summary table, we note that the permeated oxygen flux increases as we increase the percentage of fuel burned in the reactor, given that the mas flow rate is kept constant (cases R1, R2, and R3). As a result, the maximum temperature in the annular reactor also increases. When we increase the mass flow rate of the air in the tube side and keep the same mass flow rate of fuel as well as the sweeping gas (cases R4 to R10) constant, the permeated oxygen has increased, and so did the maximum temperature. This behavior will be present when there is an excess of fuel that has not been burned. Hence, the simulations can help in finding the correct amount of air mass flow rate needed to have complete combustion of the fuel.

Table 7. Simulated annulus oxy-combustion cases

Case	$V_{in,\,air}$ (m/s)	V_{fu,CO_2} (m/s)	$\%CH_4/\%CO_2$	T_{max} (K)	
R1	0.050	0.050	1.0/99.0	1.04e-7	1,213
R2	0.050	0.050	1.1/98.9	1.05e-7	1,214
R3	0.050	0.050	1.2/98.8	1.08e-7	1,214
R4	0.055	0.050	1.2/98.8	1.14e-7	1,217
R5	0.060	0.050	1.2/98.8	1.22e-7	1,220
R6	0.065	0.050	1.2/98.8	1.28e-7	1,221
R7	0.070	0.050	1.2/98.8	1.35e-7	1,224
R8	0.075	0.050	1.2/98.8	1.41e-7	1,226
R9	0.080	0.050	1.2/98.8	1.48e-8	1,228
R10	0.085	0.050	1.2/98.8	1.53e-7	1,230

According to Figure 19, where the temperature contours for four cases are shown, we note that the flame occupies a wider part of the reactor, since there is still fuel to be combusted (case R4). When the air mass flow rate is higher, it produces higher fluxes of oxygen, but the flame is shorter for the same amount of fuel (Cases R8 and R10).

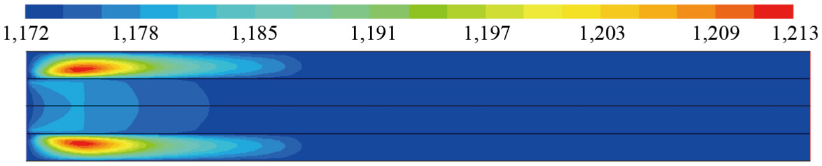

(a) Temperature contours for case R1

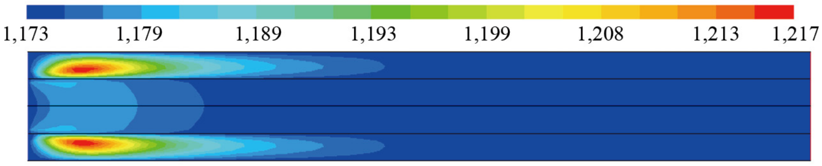

(b) Temperature contours for case R4

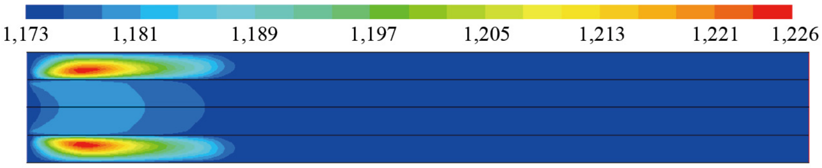

(c) Temperature contours for case R8

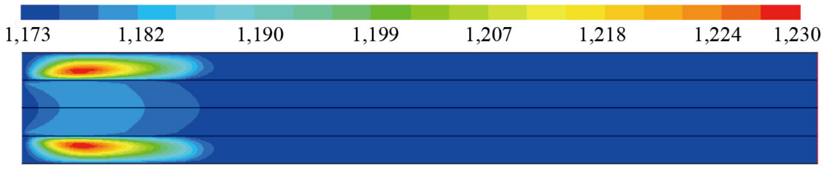

(d) Temperature contours for case R10

Figure 19. Temperature contours for annular oxy-combustion with varying air velocity

The argument becomes clearer when we look at the contours of fuel (CH_4) mass fraction (Figure 20) for the same cases depicted in Figure 19. For the lower air velocity and hence smaller mass flow rate of air, the fuel is still available for a longer part of the reactor.

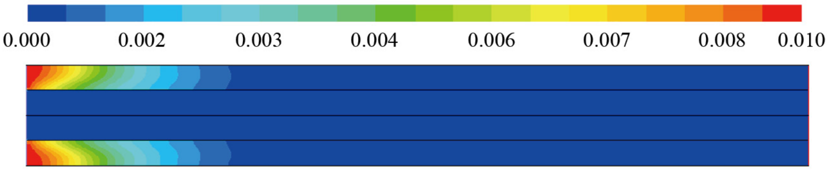

(a) CH_4 mass fraction contours for case R1

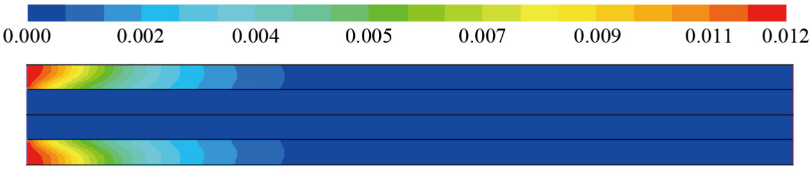

(b) CH_4 mass fraction contours for caseR4

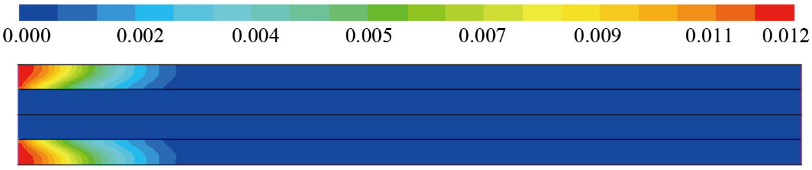

(c) CH_4 mass fraction contours for case R8

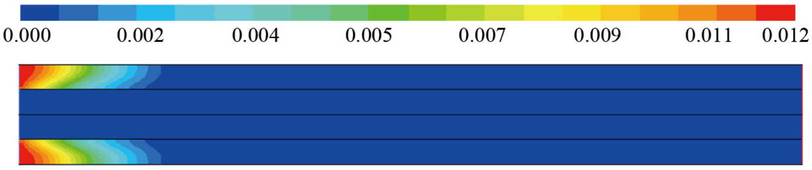

(d) CH_4 mass fraction contours for case R10

Figure 20. Methane mass fraction contours for annular oxy-combustion with varying air velocity

We can further look at the oxygen mass fraction contours for the above-discussed cases. These are presented in Figure 21. Comparing cases R1 and R4, where we have increased the fuel by 20% (from 1 to 1.2%), the flame zone became longer as the fuel needed more space to obtain the needed permeated oxygen to fully combust.

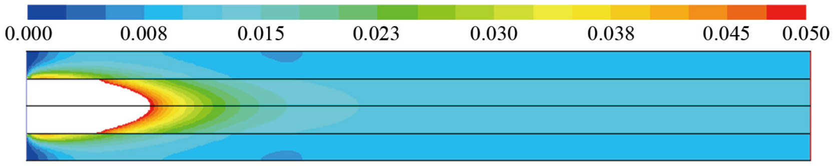

(a) O_2 mass fraction contours for case R1

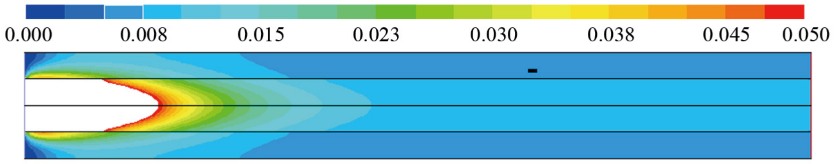

(b) O_2 mass fraction contours for case R4

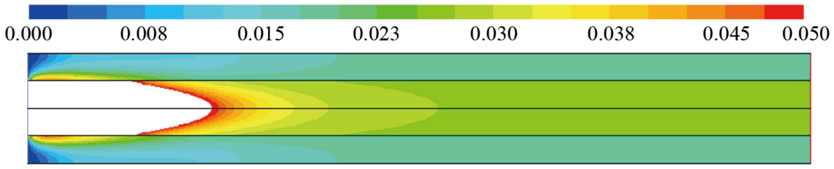

(c) O_2 mass fraction contours for case R8

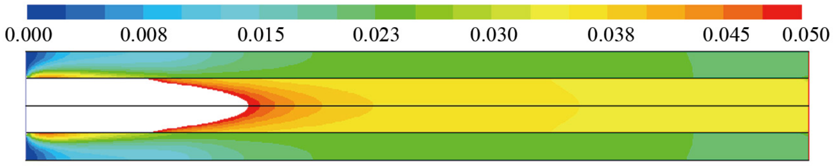

(d) O_2 mass fraction contours for case R10

Figure 21. Oxygen mass fraction contours for annular oxy-combustion with varying air velocity

By looking at the oxygen contours for cases R8 and R10, we notice that the oxygen contour levels have increased through the reactor. We have also noted that the flame length became shorter. This can be explained by the fact that the total permeated oxygen in the reactor has increased as the feeding velocity on the air side has increased. If we compare cases R1 and R10, the permeated oxygen mass flow rate across the ITM has increased by almost 50%. This was mainly a result of increasing the air feed velocity from 0.050 m/s to 0.085 m/s.

When we compare the separation case 1 (Table 5) with the annular oxy-combustion case R1 (Table 7), we note that the fuel combustion has increased the oxygen flux permeation by 17%. The amount is reasonable but is not as large as seen in stagnation flow cases (button-cell reactor), where combustion increased the flux by more than 5 times. This is because we have only used 2% methane in the reactor. We do expect much higher fluxes for higher methane feed. In addition to studying higher fuel fraction, we need to look at the scalability of the system and its operational stability. Further experimental and CFD studies are needed towards achieving these goals.

5.2.2 *Combustion inside the tube (air on annulus side)*

The following oxy-fuel combustion cases have been simulated for the case where the combustion takes place inside the tube, and we will refer to them as tubular oxy-combustion cases. Four (4) cases have been simulated and are presented in Table 8 below.

Table 8. Tube Oxy-combustion cases simulated

Case	V_{air} (m/s)(Annulus)	V_{fu,CO_2} (m/s) (tube)	$\%CH_4/\%CO_2$	Permeated O_2 mass flow rate (kg/s)	T_{max} (K)
R60	0.1	0.100	2/98	2.66e-7	1,551
R61	0.1	0.150	2/98	3.37e-7	1,577
R62	0.1	0.175	2/98	3.65e-7	1,580
R63	0.1	0.180	2/98	3.71e-7	1,581

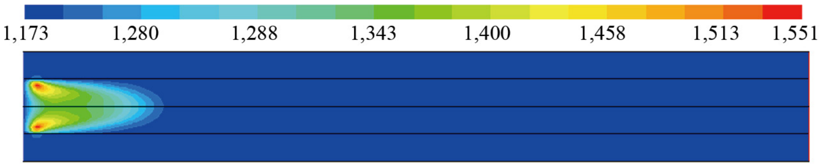

(a) Temperature contours for case R60

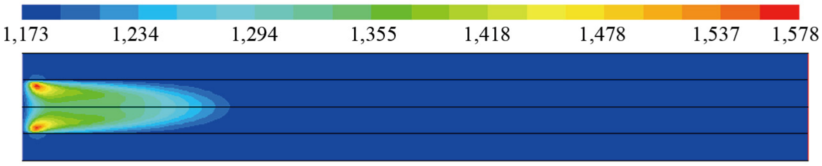

(b) Temperature contours for case R61

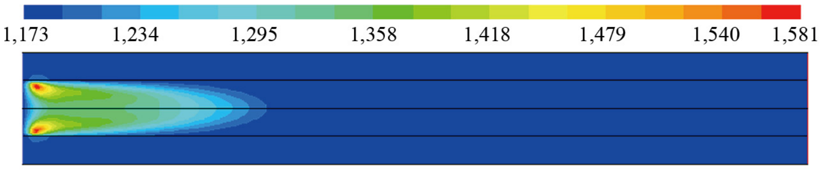

(c) Temperature contours for case R62

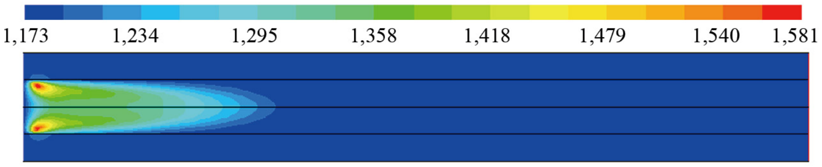

(d) Temperature contours for case R63

Figure 22. Temperature contours for tubular oxy-combustion with varying air velocity

For this limited set, we have looked at the effect of increasing the fuel/Sweeping Gas (SG: CO_2) velocity. The total permeated mass flow rate of oxygen across the ITM is listed in the column. These results show that the oxygen permeation has increased by 40% when we varied the fuel/SG velocity from 0.10 m/s to 0.18 m/s. We also note that the oxygen permeation has increased by 12% in comparison to the separation case 27 (Table 6). Hence, the effect of sweeping velocity seems to play a major role in increasing the oxygen permeation in tubular reactors.

We now look at the temperature contours for the four (4) tubular oxy-combustion cases. These contours are presented in Figure 22 above. We note that the flame length has increased as we increase the fuel/SG velocity. The flame length or the combustion zone extent is a function of many parameters. The main ones are the availability of fuel and the availability of oxygen. These contours of mass fraction of CH_4 are presented in Figure 23 below. The contours of oxygen mass fraction are shown in Figure 24.

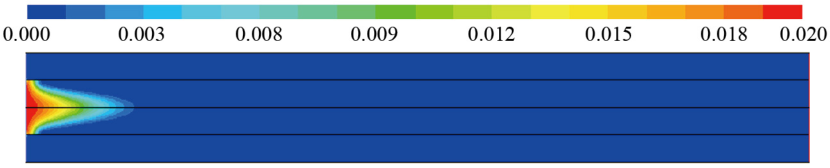

(a) CH_4 mass fraction contours for case R60

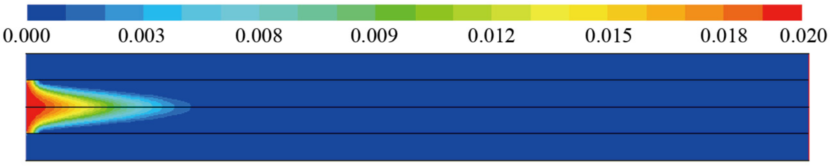

(b) CH_4 mass fraction contours for case R61

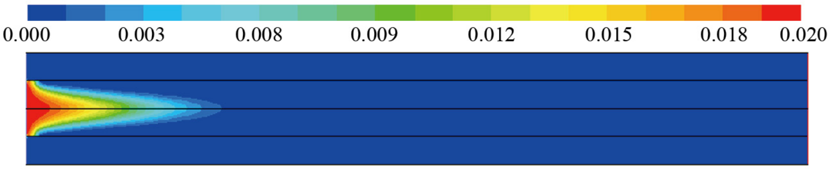

(c) CH_4 mass fraction contours for case R62

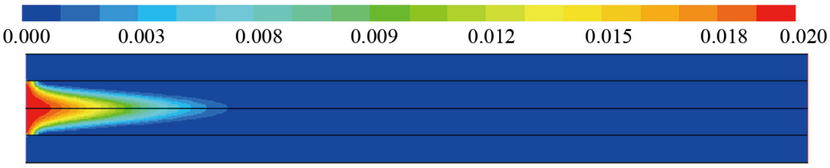

(d) CH_4 mass fraction contours for case R63

Figure 23. Methane mass fraction contours for tubular oxy-combustion with varying air velocity

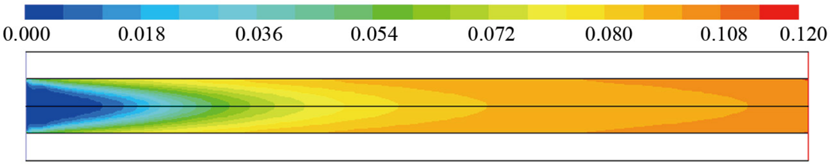

(a) O_2 mass fraction contours for case R60

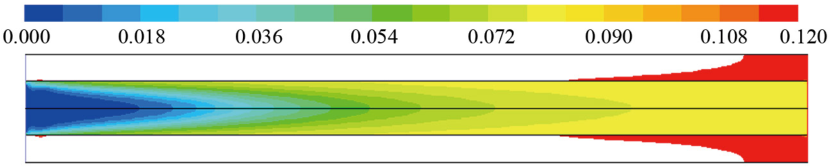

(b) O_2 mass fraction contours for case R61

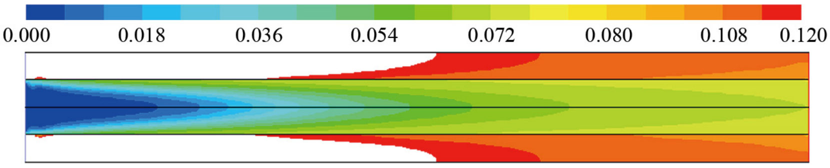

(c) O_2 mass fraction contours for case R62

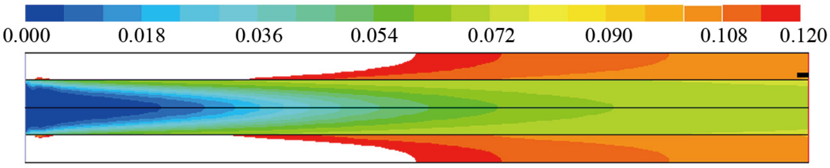

(d) O_2 mass fraction contours for case R63

Figure 24. Oxygen mass fraction contours for tubular oxy-combustion with varying air velocity

By combining the picture from the three contours (Temperature, Fuel mass fraction, and oxygen mass fraction), we gather that flame length increased, but only 8% when we increased the flow speed by almost 50%. This is because there is an excess of oxygen, which restrains the flame from getting much longer. Note also that by increasing the fuel velocity, we are also increasing the amount of fuel. This has caused the maximum temperature to increase and the extent of the hot zone of the flame to become larger inside the flame zone of each case.

In all four cases above, we managed to have excess oxygen. This has been shown experimentally (Mezghani and Hamza [14]) to increase the life of the membrane by reducing the CO_2 poising. At this juncture, we note that we have used CO_2 as a sweeping gas, and this has also been shown to poison the ITM membrane [30]. On the other hand, some research groups have worked on coming up with a stable ITM a under CO_2 environment by doping the original ITM with other metals. For example, Zhang et al. [31] have come up with a stable SFN/BSCF membrane, which was stable for a duration of 310 hours and gave 90% of the oxygen permeation given by the original BSCF membrane.

6. Conclusions

A detailed CFD model has been developed to predict the performance of two types of mini-Oxygen Transport Reactors (mOTS). The first type is a button cell type usually used to carry out laboratory experiments. The second type has a concentric tube design that can be implemented in an industrial application. Both oxygen separation and oxy-fuel combustion investigations have been carried out for both types. The results of the mathematical models have been validated using recent experimental data, and very good agreement has been found. The normalized rms value for the difference between the experimental and predicted results of the permeated oxygen for nonreactive cases was around 4%, and for the reactive cases 6% respectively.

For the **oxygen separation** investigation, the following results can be stated for the case of a 12 mm system with an inner tube diameter of 6 mm and outer tube diameter of 12 mm when the separator is operated at 1,173 K:

- It is more efficient to have the air flow in the inner tube for an air velocity ranging between 0.05 and 2 m/s.
- The effect of average sweep gas velocity is more pronounced. As the sweep velocity increased from 0.05 to 2.5 m/s, the separated oxygen mass flow rate increased by a factor of 5 or higher.
- The pressure drops on both sides of the separator and for both configurations exhibit a linear behaviour.

This study has given some important guidelines for designing and operating small oxygen ion transport separators.

For the simulated **oxy-combustion cases**, we can conclude the following:

- Ox-combustion with 2% methane fuel has increased the oxygen permeation by as much as 17% for annular oxy-combustion cases and by 12% for tubular oxy-combustion cases.
- The sweeping gas velocity increase seems to be more effective in increasing the oxygen permeation. This effect is still valid under reacting cases.
- The numerical simulation of annular oxy-combustion cases has shown great difficulty in coming up with a converged solution. Very low under-relaxation factors have been used to obtain a converged solution.

Finally, we would like to note that these simulations have been done for BSCF ITM, which may be unstable and can be poisoned if CO_2 is used as a sweeping gas or if used for a reactor case. Researchers have obtained stable and CO_2-tolerant SFN/BSCF membranes that can run for long times. These membranes have similar behaviour to BSCF and differ in permeation flux by 10%.

Acknowledgement

The author would like to acknowledge the support of the Department of Mechanical Engineering (ME), the Interdisciplinary Research Center for Sustainable Energy Systems (IRC-SES) through project INSE2526, the Research Institute (RI), and the Deanship of Research (DR) at KFUPM.

Confilict of interest

The author declares no competing financial interest.

References

[1] Binash I. *Numerical and experimental investigations of an oxy-combustion carbon free power generation system*. PhD dissertation. Dhahran, Saudi Arabia: King Fahd University of Petroleum and Minerals; 2019.

[2] Foy K, McGovern J. Comparison of ion transport membranes. In: *Fourth Annual Conference on Carbon Capture and Sequestration DOE/Netl*. Alexandria, VA, USA; 2005.

[3] Felice LD, Middelkoop V, Anzoletti V, Snijkers F, van Sint Annaland M, Gallucci F. New high temperature sealing technique and permeability data for hollow fiber BSCF perovskite membranes. *Chemical Engineering and Processing: Process Intensification*. 2016; 107: 206–219. Available from: https://doi.org/10.1016/j.cep.2014.12.004.

[4] Xu SJ, Thomson WJ. Oxygen permeation rates through ion-conducting perovskite membranes. *Chemical Engineering Science*. 1999; 54(17): 3839–3850. Available from: https://doi.org/10.1016/S0009-2509(99)00015-9.

[5] Behrouzifar A, Asadi AA, Mohammadi T, Pak A. Experimental investigation and mathematical modelling of oxygen permeation through dense $Ba_{0.5}Sr_{0.5}Co_{0.8}Fe_{0.2}O_{3-\delta}$ (BSCF) perovskite-type ceramic membranes. *Ceramics International*. 2012; 38(6): 4797–4811. Available from: https://doi.org/10.1016/j.ceramint.2012.02.068.

[6] Qi X, Lin YS, Swartz SL. Electric transport and oxygen permeation properties of lanthanum cobaltite membranes synthesized by different methods. *Industrial and Engineering Chemistry Research*. 2000; 39(3): 646–653. Available from: https://doi.org/10.1021/ie990675e.

[7] Yang Z, Lin YS. A semi-empirical equation for oxygen nonstoichiometry of perovskite-type ceramics. *Solid State Ionics*. 2002; 150(3–4): 245–254. Available from: https://doi.org/10.1016/S0167-2738(02)00524-6.

[8] Wang H, Cong Y, Yang W. Oxygen permeation study in a tubular $Ba_{0.5}Sr_{0.5}Co_{0.8}Fe_{0.2}O_{3-\delta}$ oxygen permeable membrane. *Journal of Membrane Science*. 2002; 210(2): 259–271. Available from: https://doi.org/10.1016/S0376-7388(02)00361-7.

[9] van Hassel BA. Oxygen transfer across composite oxygen transport membranes. *Solid State Ionics*. 2004; 174(1–4): 253–260. Available from: https://doi.org/10.1016/j.ssi.2004.07.034.

[10] Liu S, Gavalas GR. Oxygen selective ceramic hollow fiber membranes. *Journal of Membrane Science*. 2005; 246(1): 103–108. Available from: https://doi.org/10.1016/j.memsci.2004.09.028.

[11] Tan X, Pang Z, Li K. Oxygen production using $La_{0.6}Sr_{0.4}Co_{0.2}Fe_{0.8}O_{3\delta}$ (LSCF) perovskite hollow fibre membrane modules. *Journal of Membrane Science*. 2008; 310(1–2): 550–556. Available from: https://doi.org/10.1016/j.memsci.2007.11.051.

[12] Mancini ND, Mitsos A. Ion transport membrane reactors for oxy-combustion-Part II: Analysis and comparison of alternatives. *Energy*. 2011; 36(8): 4721–4739. Available from: https://doi.org/10.1016/j.energy.2011.05.024.

[13] Liu J, Zhao J, Liu Y, Zhu Y, Zhou W, Gu Z, et al. Research progress of computational fluid dynamics in mixed ionic-electronic conducting oxygen-permeable membranes. *Membranes*. 2025; 15(7): 193. Available from: https://doi.org/10.3390/membranes15070193.

[14] Mezghani K, Hamza A. Application of $Ba_{0.5}Sr_{0.5}Co_{0.8}Fe_{0.2}O_{3-\delta}$ membranes in an oxy-fuel combustion reactor. *Journal of Membrane Science*. 2016; 518: 254–262. Available from: https://doi.org/10.1016/j.memsci.2016.07.001.

[15] Kirchen P, Apo DJ, Hunt A, Ghoniem AF. A novel ion transport membrane reactor for fundamental investigations of oxygen permeation and oxy-combustion under reactive flow conditions. *Proceedings of the Combustion Institute*. 2013; 34(2): 3463–3470. Available from: https://doi.org/10.1016/j.proci.2012.07.076.

[16] Ben-Mansour R. Effect of flow and geometric configuration on oxygen separation productivity of ion transport membranes. In: *14th International Conference on Heat Transfer, Fluid Mechanics and Thermodynamics*. Wicklow, Ireland; 2019. p.167–172.

[17] Ben-Mansour R, Habib MA, Badr HM, Azharuddin, Nemitallah M. Characteristics of oxy-fuel combustion in an oxygen transport reactor. *Energy and Fuels*. 2012; 26(7): 4599–4606. Available from: https://doi.org/10.1021/ef300539c.

[18] Farooqui AE, Badr HM, Habib MA, Ben-Mansour R. Numerical investigation of combustion characteristics in an oxygen transport reactor. *International Journal of Energy Research*. 2014; 38: 638–651. Available from: https://doi.org/10.1002/er.3070.

[19] Ansys Inc. *Ansys Fluent user manual, theoretical part, version (2006)*. Canonsburg, PA: Ansys Inc.; 2006. Available from: https://ansyshelp.ansys.com/public/account/secured?returnurl=/Views/Secured/corp/v242/en/flu_ug/flu_ug.html [Accessed 1st March 2026].

[20] Fox RW, McDonald AT. *Introduction to Fluid Mechanics*. 4th ed. New York: John Wiley & Sons; 1992.

[21] Incropera FP, Dewitt DP, Bergman TL, Lavine AS. *Fundamentals of Heat and Mass Transfer*. 6th ed. Hoboken, NJ: John Wiley & Sons; 2007.

[22] Siegel R, Howell JR. *Thermal Radiation Heat Transfer*. 4th ed. New York: Taylor and Francis; 2002.

[23] Smith TF, Shen ZF, Friedman JN. Evaluation of coefficients for the weighted sum of gray gases model. *Journal of Heat Transfer*. 1982; 104(4): 602–608. Available from: https://doi.org/10.1115/1.3245174.

[24] Rajhi MA, Ben-Mansour R, Habib MA, Nemitallah MA, Andersson K. Evaluation of gas radiation models in CFD modelling of oxy-combustion. *Energy Conversion and Management*. 2014; 81: 83–97. Available from: https://doi.org/10.1016/j.enconman.2014.02.019.

[25] Anderson Jr JD. *Computational Fluid Dynamics*. Berlin, Heidelberg: Springer Berlin Heidelberg; 2009.

[26] Ra Y, Chuahy F, Kokjohn S. Development and validation of a reduced reaction mechanism with a focus on diesel fuel/syngas co-oxidation. *Fuel*. 2016; 185: 663–683. Available from: https://doi.org/10.1016/j.fuel.2016.07.039.

[27] Westbrook CK, Dryer FL. Simplified reaction mechanisms for the oxidation of hydrocarbon fuels in flames. *Combustion Science and Technology*. 1981; 27(1–2): 31–43. Available from: https://doi.org/10.1080/00102208108946970.

[28] Yin C, Rosendahl LA, Kær SK. Chemistry and radiation in oxy-fuel combustion: A computational fluid dynamics modeling study. *Fuel*. 2011; 90(7): 2519–2529. Available from: https://doi.org/10.1016/j.fuel.2011.03.023.

[29] Patankar S. *Numerical Heat Transfer and Fluid Flow*. 1st ed. Boca Raton, FL: CRC Press; 1980.

[30] Arnold M, Wang H, Feldhoff A. Influence of CO_2 on the oxygen permeation performance and the microstructure of perovskite-type $(Ba_{0.5}Sr_{0.5})$-$(Co_{0.8}Fe_{0.2})$ $O_{3-\delta}$ membranes. *Journal of Membrane Science*. 2007; 293(1): 44–52. Available from: https://doi.org/10.1016/j.memsci.2007.01.032.

[31] Zhang Z, Chen D, Gao Y, Yang G, Dong F, Chen C, et al. A CO_2-tolerant nanostructured layer for oxygen transport membranes. *RSC Advances*. 2014; 4(49): 25924–25932. Available from: https://doi.org/10.1039/C4RA03028A.